Taxel-Addressable Matrix of Vertical-Nanowire Piezotronic Transistors for Active and Adaptive Tactile Imaging

Wenzhuo Wu *et al.*

Science **340**, 952 (2013);
DOI: 10.1126/science.1234855

SS Cygni back in line with that expected for systems of similar orbital period (*21*).

Our revised distance also tests a second prediction of the DIM: The mass accretion rate at the onset of the outburst decline should be very close to the critical rate. The mass accretion rate predicted by the DIM was approximated by (*7*) to have a power-law dependence on several key system parameters (the distance, inclination angle, disc size, white dwarf mass, and apparent magnitude). For a distance of 114 pc and the range of system parameters derived by (*22*), this approximation predicts an apparent visual magnitude in the range 8.8 to 9.5 at the onset of decline, as compared to the observed value of ~8.6. If the DIM is correct, and the approximation of (*7*) is valid in the revised region of parameter space, this implies that the inclination angle of the system must be close to 45°, and the mass of the white dwarf should be close to the mass of the Sun.

Besides CVs, the DIM has been used to explain the main features of XRB outbursts, when modified to account for the heating effect of x-ray irradiation (*23*) and the truncation of the inner disc (*24*). The thermal-viscous instability at the heart of the DIM is also believed to be active in AGN (*25*), although in that case it only produces relatively small amplitude variability rather than large outbursts (*26*). In an exact parallel to the distinction between dwarf novae and nova-like CVs, the difference between transient and persistent XRBs is attributed to mass transfer rates either below or above a critical threshold (*10*, *11*). A failure of this model in SS Cygni would therefore have called into question our understanding not only of dwarf novae but of transient XRBs.

The controversy over the distance to SS Cygni emphasizes the need for accurate distances to accreting objects. Since they use stationary reference frames, VLBI parallax studies can play a critical role in determining the distance to radio-emitting Galactic sources, especially now that recent sensitivity upgrades to VLBI instruments have enabled the extension of such studies to a larger population of sources.

References and Notes

1. J.-P. Lasota, *New Astron. Rev.* **45**, 449 (2001).
2. J. K. Cannizzo, J. A. Mattei, *Astrophys. J.* **401**, 642 (1992).
3. M. R. Schreiber, J.-M. Hameury, J.-P. Lasota, *Astron. Astrophys.* **410**, 239 (2003).
4. T. E. Harrison *et al.*, *Astron. J.* **515**, L93 (1999).
5. T. E. Harrison, B. J. McNamara, P. Szkody, R. L. Gilliland, *Astron. J.* **120**, 2649 (2000).
6. T. E. Harrison *et al.*, *Astron. J.* **127**, 460 (2004).
7. M. R. Schreiber, B. T. Gänsicke, *Astron. Astrophys.* **382**, 124 (2002).
8. M. R. Schreiber, J.-P. Lasota, *Astron. Astrophys.* **473**, 897 (2007).
9. J.-P. Lasota, *New Astron. Rev.* **51**, 752 (2008).
10. J. van Paradijs, *Astrophys. J.* **464**, L139 (1996).
11. M. Coriat, R. P. Fender, G. Dubus, *Mon. Not. R. Astron. Soc.* **424**, 1991 (2012).
12. J. Smak, *Acta Astron.* **60**, 83 (2010).
13. J.-P. Lasota, *Mem. Soc. Astron. Ital.* **83**, 469 (2012).
14. E. Körding *et al.*, *Science* **320**, 1318 (2008).
15. See supplementary materials on *Science* Online.
16. T. E. Lutz, D. H. Kelker, *Publ. Astron. Soc. Pac.* **85**, 573 (1973).
17. C. Koen, *Mon. Not. R. Astron. Soc.* **256**, 65 (1992).
18. N. Zacharias *et al.*, *Astron. J.* **145**, 44 (2013).
19. R. C. North, T. R. Marsh, U. Kolb, V. S. Dhillon, C. K. J. Moran, *Mon. Not. R. Astron. Soc.* **337**, 1215 (2002).
20. T. Ak, S. Bilir, S. Ak, K. B. Coşkunoğlu, Z. Eker, *New Astron.* **15**, 491 (2010).
21. J. Patterson, *Mon. Not. R. Astron. Soc.* **411**, 2695 (2011).
22. M. A. Bitner, E. L. Robinson, B. B. Behr, *Astrophys. J.* **662**, 564 (2007).
23. A. R. King, H. Ritter, *Mon. Not. R. Astron. Soc.* **293**, L42 (1998).
24. G. Dubus, J.-M. Hameury, J.-P. Lasota, *Astron. Astrophys.* **373**, 251 (2001).
25. D. N. C. Lin, G. A. Shields, *Astrophys. J.* **305**, 28 (1986).
26. J.-M. Hameury, M. Viallet, J.-P. Lasota, *Astron. Astrophys.* **496**, 413 (2009).

Acknowledgments: We thank the amateur astronomers of AAVSO, whose optical monitoring of SS Cygni was crucial for triggering our radio observations, and J. Thorstensen and A. Deller for useful discussions. Supported by the Australian Research Council's Discovery Projects funding scheme (J.C.A.M.-J. and G.R.S.; project DP120102393), a Discovery Grant from the Natural Sciences and Engineering Research Council of Canada (G.R.S.), a Consolidated Grant from the UK Science and Technology Facilities Council to the Southampton Astronomy Group (C.K.), and a VIDI grant from NWO, the Netherlands Organisation for Scientific Research (E.G.K.; grant 016.123.356). The data reported in this paper are tabulated in the supplementary materials. The National Radio Astronomy Observatory is a facility of NSF operated under cooperative agreement by Associated Universities Inc. The European VLBI Network is a joint facility of European, Chinese, South African, and other radio astronomy institutes funded by their national research councils. This work made use of the Swinburne University of Technology software correlator, developed as part of the Australian Major National Research Facilities Programme and operated under license.

Supplementary Materials

www.sciencemag.org/cgi/content/full/340/6135/950/DC1
Supplementary Text
Fig. S1
Tables S1 and S2
References (*27*–*33*)

27 February 2013; accepted 25 April 2013
10.1126/science.1237145

Taxel-Addressable Matrix of Vertical-Nanowire Piezotronic Transistors for Active and Adaptive Tactile Imaging

Wenzhuo Wu,[1]* Xiaonan Wen,[1]* Zhong Lin Wang[1,2]†

Designing, fabricating, and integrating arrays of nanodevices into a functional system are the key to transferring nanoscale science into applicable nanotechnology. We report large-array three-dimensional (3D) circuitry integration of piezotronic transistors based on vertical zinc oxide nanowires as an active taxel-addressable pressure/force sensor matrix for tactile imaging. Using the piezoelectric polarization charges created at a metal-semiconductor interface under strain to gate/modulate the transport process of local charge carriers, we designed independently addressable two-terminal transistor arrays, which convert mechanical stimuli applied to the devices into local electronic controlling signals. The device matrix can achieve shape-adaptive high-resolution tactile imaging and self-powered, multidimensional active sensing. The 3D piezotronic transistor array may have applications in human-electronics interfacing, smart skin, and micro- and nanoelectromechanical systems.

Progress has been achieved in implementing flexible pressure sensors based on arrays of tactile pixels (taxels) for mimicking the tactile sensing capabilities of human skin. In these sensors, electronic components such as traditional planar field-effect transistors (FETs) act as readout elements for detecting pressure-induced property changes in the pressure-sensitive media (*1*–*6*). Their continued improvement depends on minimizing the effect of substrate strain on the performance of the electronic components while increasing the flexibility of the substrate (*1*–*3*, *7*). This scheme of pressure sensing not only requires complicated system integration of heterogeneous components but also lacks direct and active interfacing between electronics and mechanical actuations. Moreover, the sizes of as-fabricated taxels are hundreds of micrometers to tens of millimeters, severely limiting device density and spatial resolution. Although architectures such as three-dimensional (3D) integrated circuits and wrap-gate vertical transistors present attractive approaches to achieving high-density assembly of functional nanodevices (*8*–*11*), it is cumbersome to fabricate the gate electrode and manage the interconnect layout so as to effectively control an individual device within a high-density matrix. A schematic of a representative wrap-gate nanowire (NW) FET is shown in Fig. 1A.

Recently, using piezoelectric semiconductor NWs that typically have wurtzite and zinc blend structures (such as ZnO and GaN), a piezotronic transistor design was introduced (*12*–*15*) that has a two-terminal metal-semiconductor-metal structure and whose charge carrier transport is modulated by the piezoelectric polarization charge–

[1]School of Materials Science and Engineering, Georgia Institute of Technology, Atlanta, GA 30332, USA. [2]Beijing Institute of Nanoenergy and Nanosystems, Chinese Academy of Sciences, Beijing 100083, China.

*These authors contributed equally to this work.
†Corresponding author. E-mail: zhong.wang@mse.gatech.edu

induced inner-crystal potential in the NW at the contacts. The piezotronic effect differs from the conventionally used piezoresistive effect in that the latter results from a change in band gap, charge carrier density, or density of states in the conduction band of the strained semiconductor material (which functions as a scalar "resistor"), whereas the piezotronic effect arises as a result of the polarization of nonmobile ions in the crystal. Therefore, the piezoresistive effect is a symmetric volume effect without polarity, whereas the piezotronic effect is an interface effect that asymmetrically modulates local contacts at different terminals of the device because of the polarity of the piezoelectric potential (piezopotential) (*15*–*18*). The magnitude and polarity of piezopotential within a piezotronic transistor changes according to the local stress or force, resulting in a direct control over local Schottky barrier heights (SBHs) and hence the corresponding transport characteristics of the piezotronic transistor by induced strain. Consequently, no applied electrical gate voltage is required for a piezotronic transistor. Strain-gated piezotronic transistors operate through the modulation of local contact characteristics and charge carrier transport by strain-induced ionic polarization charges at the interface of a metal-semiconductor contact (*13*, *16*–*20*), which is different from the voltage-gated operation of a traditional FET.

The elimination of a wrap gate also offers a new approach for 3D structuring. The basic structure of a 3D strain-gated vertical piezotronic transistor (SGVPT) (Fig. 1A, right) consists of one or more vertically grown ZnO NWs in contact with bottom and top electrodes. Each ZnO NW experiences axial strain when subjected to external mechanical deformation, with piezopotential induced inside the NW as a result of polarization of nonmobile ions distributed at the two ends (*15*, *17*, *18*). The local contact profile and carrier transport characteristics across the Schottky barrier, formed between the ZnO NW and metal electrodes, is effectively controlled by the polarization charge–induced potential. The electrical characteristics of the two-terminal SGVPT are therefore modulated by external mechanical actions induced by strain; that is, strain essentially functions as a gate signal for controlling the SGVPT.

By combining the patterned in-place growth of vertically aligned ZnO NWs with state-of-the-art microfabrication techniques, large-scale integration of a SGVPT array can be obtained. Figure 1B illustrates a 1-cm^2 SGVPT array with a taxel density of 92 × 92 (234 taxels per inch). The

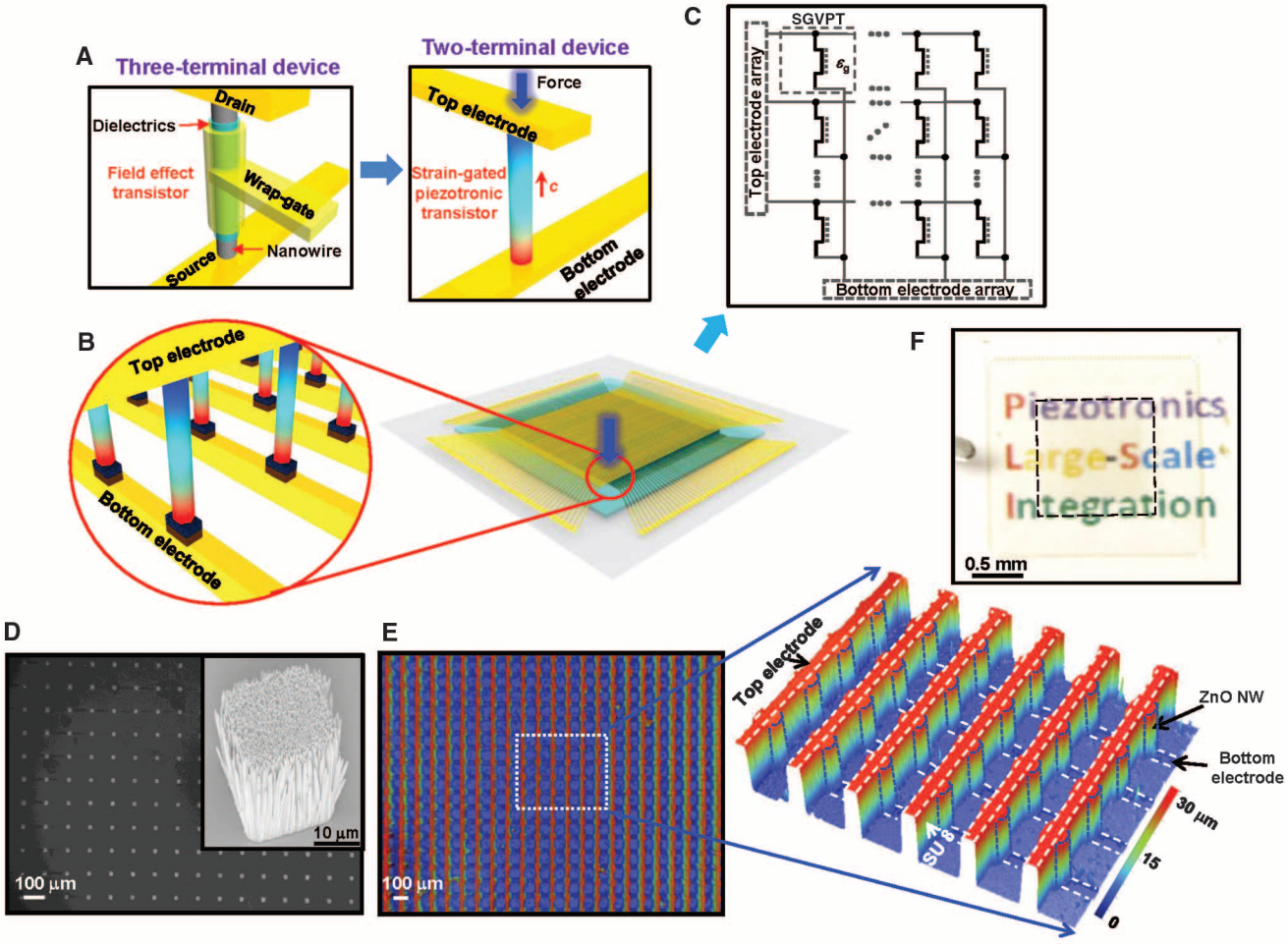

Fig. 1. Schematic illustration, optical and electron microscopic images, and topological profile image of 3D SGVPT array assembly. (**A**) Comparison between three-terminal voltage-gated NW FET (left) and two-terminal strain-gated vertical piezotronic transistor (right). Color gradient in the strained SGVPT represents the strain-induced piezopotential field, in which red and blue indicate positive and negative piezopotential, respectively. ZnO NWs in SGVPT grow along the *c* axis (red arrow). (**B**) Schematic illustration of a 3D SGVPT array with taxel density of 92 × 92 and scheme for spatial profile imaging of local stress (indicated by the downward blue arrow) by the array (zoom-in schematic). (**C**) Equivalent circuit diagram of the 3D SGVPT array. The region highlighted by black dashed lines is the unit SGVPT device, in which ε_g represents the mechanical strain gate signal and the vertical dotted line between the two terminals of the SGVPT denotes the modulation effect of ε_g on the conducting characteristics of the device. (**D**) Scanning electron micrograph of SGVPT array taken after etching back the SU 8 layer and exposing top portions (~20 μm) of the ZnO NWs. Inset shows 30°-tilt view of the exposed ZnO NWs for a single taxel. (**E**) Topological profile image of the SGVPT array (top view). At right, a 3D perspective view of the topological profile image reveals the vertical hierarchy of the SGVPT assembly; the color gradient represents different heights, as indicated. (**F**) Optical image of the transparent 3D SGVPT array on a flexible substrate. The peripherals are the pads of the device, and the central region highlighted by black dashed lines is the active array of 3D SGVPTs.

equivalent circuit diagram of the SGVPT (Fig. 1C) shows the operation scheme of the SGVPT device circuitry. The taxel area density of the SGVPT array is 8464 cm^{-2}, which is higher than the number of tactile sensors in recent reports (~6 to 27 cm^{-2}) (*1*–*3*, *6*) and mechanoreceptors embedded in human fingertip skin (~240 cm^{-2}) (*21*). A detailed description of the device fabrication process is shown in the supplementary materials and figs. S1 and S2. Briefly, the active array of SGVPTs is sandwiched between the top and bottom indium tin oxide (ITO) electrodes, which are aligned in orthogonal cross-bar configurations. A thin layer of Au is deposited between the top and bottom surfaces of ZnO NWs and the top and bottom ITO electrodes, respectively, forming Schottky contacts with ZnO NWs. A thin layer of Parylene C (SCS Labcoter; thickness 1 μm) is conformably coated on the SGVPT device as the moisture and corrosion barrier. Well-aligned ZnO NWs, synthesized by a low-temperature hydrothermal method (*22*), function as the active channel material of the SGVPT and help reduce the stochastic taxel-to-taxel variation to ensure uniform device performance. Figure 1D and fig. S3 show the SGVPT array after etching back the encapsulation SU 8 layer (epoxy-based negative photoresist) and exposing the top portions (~20 μm) of the ZnO NWs (see supplementary materials for fabrication details). The as-synthesized ZnO NWs show single crystallinity (fig. S3).

The 3D nature and vertical hierarchy of the SGVPT assembly is revealed by topological profile imaging (Fig. 1E) using an optical noncontact profilometer (Wyko Profilometer NT3300), which measures the phase change of light reflected from various heights in the structure by interferometry. The high degree of alignment and uniformity of the SGVPT array in three dimensions (~30 μm in height, 20 μm × 20 μm in taxel size) is enabled by process control in both the bottom-up synthesis of NWs and the top-down fabrication of circuitry. The use of a two-terminal configuration based on the piezotronic effect simplifies the layout design and circuitry fabrication while maintaining effective control over individual devices. The transparency and flexibility of SGVPT array devices are shown in Fig. 1F and figs. S4 and S5.

By selecting one top electrode, the 92 taxels between this top electrode and the corresponding bottom electrodes can be addressed and characterized individually (see supplementary materials). Representative data from 23 taxels in a typical single-channel line scan (1 × 92) measurement for a SGVPT array device are shown in Fig. 2. The corresponding topological profile images (top view) of the selected taxels are displayed at

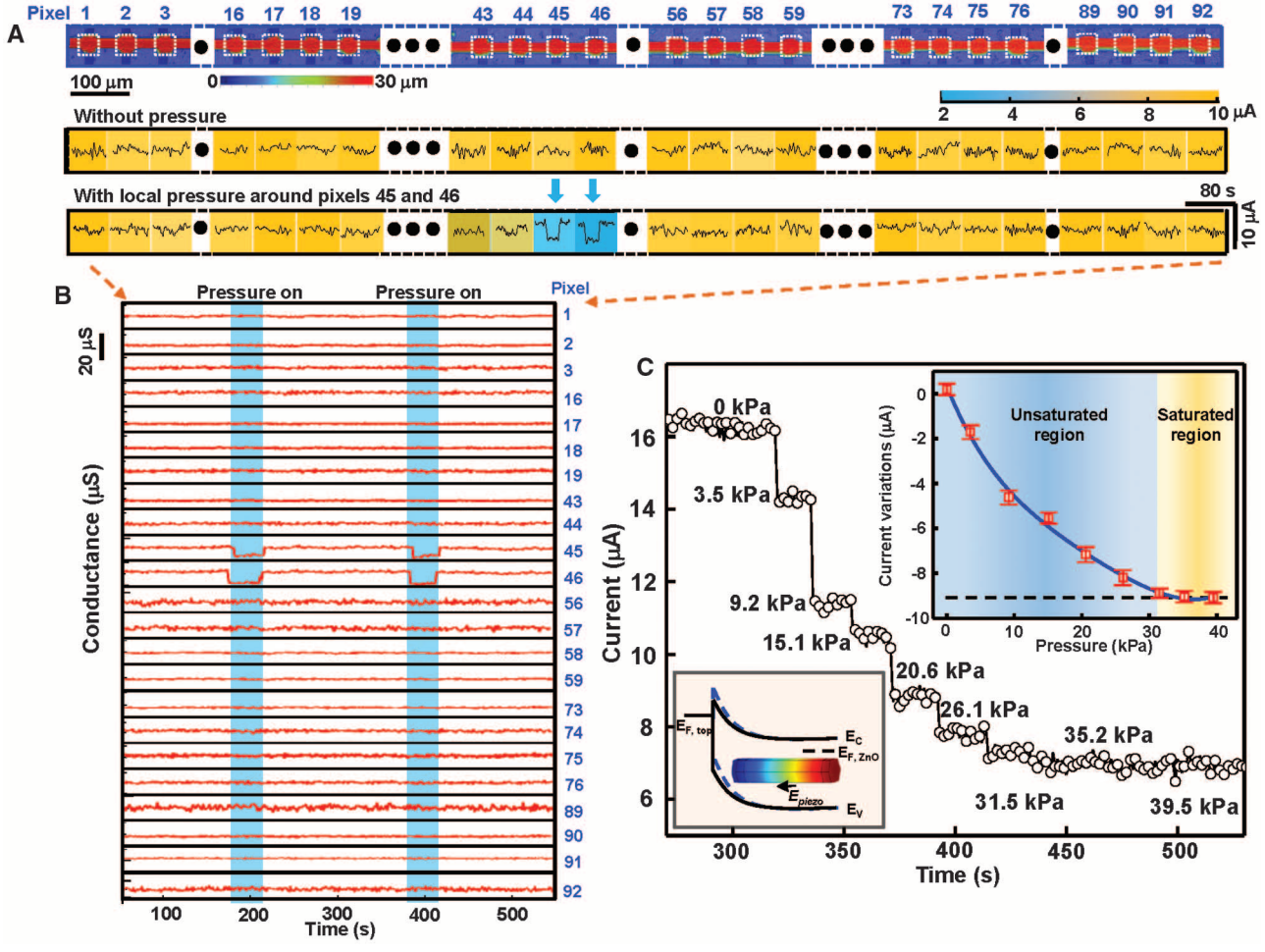

Fig. 2. Single-channel line scan (1 × 92) electrical measurement for SGVPT array device. (**A**) Topological profile images (top view) of 23 selected taxels in a 1 × 92 SGVPT array (single channel; top frame) and their corresponding current responses (middle and bottom frames) under 1 V bias without and with external stress (20 kPa) applied to a localized region around taxels 45 and 46. (**B**) Single-channel conductance measurement in the temporal domain, illustrating the dynamic response of the 23 selected SGVPT devices in this channel, without and with pressure applied. (**C**) Current responses for taxel 46 under different pressures, showing the gate modulation effect of applied pressure on the electrical characteristics of the SGVPT. Top right inset: Current variations (red squares) are plotted versus the applied pressures, clearly showing the saturation of current change when applied pressure is above ~30 kPa. Bottom left inset: Schematic band diagram illustrating the change in SBH of the reverse-biased top contact due to the modulation effect of strain-induced piezopotential. Color gradient represents the distribution of piezopotential field (red indicates positive piezopotential; blue indicates negative piezopotential). The original band edges at the reverse-biased Schottky contact for the SGVPT device without stress applied are shown as black solid lines. The band edges bending at the reverse-biased Schottky contact for the SGVPT device with stress applied are shown as blue dashed lines.

the top of Fig. 2A. The current response from each taxel under 1 V bias, with and without external pressure (20 kPa) applied to a localized region (around taxels 45 and 46), is recorded and plotted, with colors representing the ratio of the response amplitude for each taxel in an 80-s window. It can be seen that for this single-channel array of SGVPTs, pressure variations can be distinguished with both high sensitivity and spatial resolution (taxel periodicity, ~100 μm). The dominant mechanism for the transport property of SGVPT is the piezotronic effect rather than the piezoresistance effect, as experimentally confirmed and elaborated (fig. S6) (*15*, *17*, *18*). Data from single-channel conductance measurements in the temporal domain are compiled and shown in Fig. 2B and fig. S7 to further illustrate the dynamic response of SGVPT devices. Distinctive changes in conductance can be observed for taxels 45 and 46 before and after applying the localized pressure. Although the measured response time (rise time) of ~0.15 s for a SGVPT taxel (fig. S7) is larger than that of human fingertips (~30 to 50 ms), it is comparable to previously reported values of 0.1 s (*1*). These results indicate that a SGVPT array can respond to static as well as dynamic stimuli. The response time can be further improved in future designs by integrating local on-site signal processing circuits with a SGVPT array (*23*).

The pressure sensitivity of a single SGVPT is shown in Fig. 2C for taxel 46. We applied increasing pressure at a fixed location on the SGVPT and measured the variations in current response. The SGVPT device demonstrated high sensitivity for detecting pressure change, particularly in low-pressure regions (<10 kPa). A plot of current variation versus pressure change (Fig. 2C, top right inset) shows the modulation effect of applied pressure. It can be seen that the maximum pressure at which a SGVPT taxel can still distinguish without "saturation" is around 30 kPa, above which the current saturates. The observed sensing range of a few kPa to ~30 kPa for a SGVPT array is well matched to the range of pressure that a human finger applies to sense texture and shape, 10 to 40 kPa (*24*). The sensitivity of a SGVPT, defined as $S = dG_{SGVPT}/dP$ (where G is the measured conductance for SGVPT), is around 2.1 μS kPa^{-1}; this value arises from the change in carrier transport of the SGVPT by applied pressure due to the corresponding modulation of barrier height at the reverse-biased Schottky contact by strain-induced piezopotential (*15*, *17*, *18*).

The conductance of a SGVPT device is dictated by the reverse-biased Schottky contact, which is formed between ZnO NWs and top electrodes in this case. Upon applying the normal stress, accumulation of piezoelectric charges at both Schottky contacts induces the distribution of piezopotential. Because of the orientation of the polar *c* axis in the as-synthesized ZnO NWs (red arrow in Fig. 1A, right panel), negative piezopotential is induced at the reverse-biased top Schottky contact, which raises the barrier height at that contact and hence decreases the transport conductance of the SGVPT taxel, as depicted by the schematic band diagrams in Fig. 2C (bottom left inset) and fig. S6. The operation of the SGVPT device is therefore based on barrier-interface modulation that enables enhanced sensitivity and efficiency relative to the channel modulation operation in conventional FETs. The quality of the Schottky contacts has been characterized (supplementary materials and fig. S8). The SBHs and ideality factors of the formed contacts for devices without extra oxygen plasma treatment before depositing the top electrode are 0.419 ± 0.011 eV and 5.84 ± 1.29, respectively, whereas the SBHs and ideality factors of the formed contacts for devices with extra oxygen plasma treatment before depositing the top electrode are found to be 0.575 ± 0.013 eV and 2.17 ± 0.33, respectively. These results indicate that the qualities of as-fabricated Schottky contacts have been improved by the oxygen plasma treatment (*19*).

The feasibility and scalability of the proposed integration scheme are demonstrated by the successful fabrication of the 92 × 92-taxel SGVPT array, enabling a factor of 15 to 25 increase in number of taxels and a factor of 300 to 1000 increase in taxel area density relative to recent reports (*1*–*3*, *6*). The output current of each individual SGVPT taxel is measured and averaged within a short duration window of 10 ms. By monitoring the output current of each independently functioning SGVPT in the matrix, a spatial profile of applied pressure can be readily imaged by multiplexed addressing of all the taxels. A 2D current contour plot was thus obtained by registering the measured current to the corresponding taxel coordinates along the *x* (bottom electrode) and *y* (top electrode) axes. Metrology mapping was then performed on the fully integrated SGVPT array without applying pressure (Fig. 3A, inset), demonstrating that all of the 8464 SGVPTs within the array are functional. Subsequent statistical investigation revealed good uniformity in electrical characteristics among all taxels, with 95% of the SGVPTs possessing current values in the narrow range of 13.7 ± 2.73 μA under 1 V bias (Fig. 3A). The uniformity in the current distribution of SGVPTs can be further improved by optimizing the fabrication process, such as achieving a uniform number of ZnO NWs within each taxel (fig. S3) and obtaining even profiles in the etch-back step of

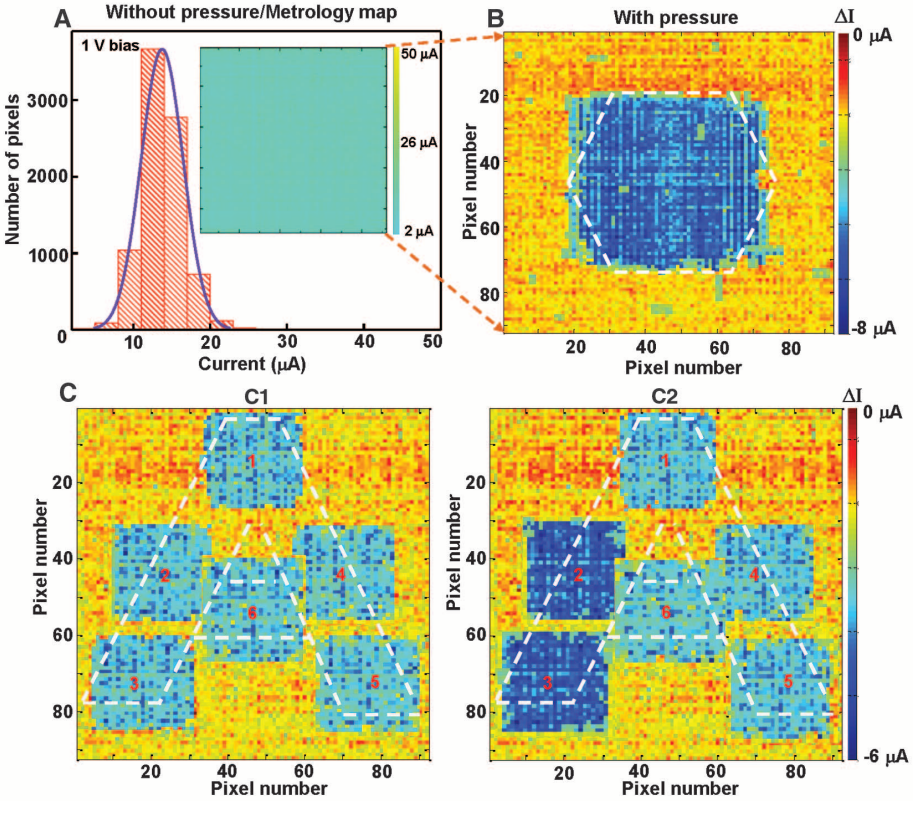

Fig. 3. Tactile imaging and multidimensional sensing by the fully integrated 92 × 92 SGVPT array. (**A**) Metrology mapping (inset) and statistical investigation of the fully integrated SGVPT array without applying stress. (**B**) Current response contour plot illustrating the capability of SGVPT array for imaging the spatial profile of applied stress. Color scale represents the current differences for each taxel before and after applying the normal stress. The physical shape of the applied stress is highlighted by the white dashed lines. (**C**) Multidimensional sensing by an SGVPT array exhibits the potential of realizing applications such as personal signature recognition with maximum security and unique identity. The shape of a "written" letter A is highlighted by the white dashed lines.

the SU 8 layer. To demonstrate the tactile sensing capability of the integrated SGVPT array, we applied a normal stress of ~25 kPa to the device by pressing a hexagonal mold. As shown in Fig. 3B, which presents for each taxel the difference between current values before and after applying the normal stress, the profile of applied stress can be spatially imaged.

The SGVPT devices remained operational and capable of imaging the spatial profile of applied pressure after 24 hours of immersion in 23°C deionized water and 37°C 0.9% saline solution, as well as after 6 hours of immersion in 65°C deionized water and 65°C 0.9% saline solution (figs. S9 and S10), indicating good stability and feasibility of SGVPT array operation for future applications such as in vivo physiological sensing in complex environments. Deteriorated adhesion between the encapsulation SU 8 layer in the SGVPT array and the substrate was observed for devices after prolonged immersion (12 hours) in both solutions at 65°C. Note that even in such cases, the top electrodes and taxels remained in good shape; only rupture of the bottom electrodes can be seen (fig. S10).

To investigate whether a single device array could resolve the stress profile spatially while also registering the stress variations to the mapped geometrical pattern (as enabled by the uniform sensitive response of taxels across the whole array and the high spatial taxel density), we used a SGVPT device (Fig. 3C) fabricated on a solid silicon substrate. A three-axis stage and force gauge was used to apply normal stresses with well-determined values and spatial locations to the device (see supplementary materials). The first group of six normal local stresses, each around 8.1 kPa, were applied to the array at preprogrammed locations in a sequence indexed from 1 to 6, with the corresponding contours imaged and organized (Fig. 3C, panel C1) to emulate the process of writing the letter A. This process was achieved by varying the x and y coordinates while keeping the z coordinate constant in the control interface of the three-axis stage. It can be seen from Fig. 3C (panel C1) that spatial profiles of all six applied stresses can be distinguished and mapped electronically. The second group of six normal stresses with the same locations were then applied to the array in the same sequence, except that the stresses applied at sites 2 and 3 were increased to ~20 kPa; stresses at the other four sites were unchanged. The corresponding mapped contours were again recorded and organized (Fig. 3C, panel C2). These results demonstrate the potential of using an SGVPT array for future applications such as multidimensional signature recording, which not only records the calligraphy or signature patterns when people write, but also registers the corresponding pressure or force applied at each location (dictated by the resolution of the taxel array) by the writer. This augmented capability enables personal signature recognition with unique identity and enhanced security.

The real-time detection of shape changes caused by stretching or twisting is a desirable feature for sensors embedded in an artificial tissue or prosthetic device. Figure 4A shows the experimental setup for investigating the feasibility of a SGVPT array for shape-adaptive sensing. A rectangular supporting object is affixed to the platen of probe station, directly beneath the central region of the SGVPT array. After the probe pins are in contact with the pads at the periphery of the SGVPT device, the platen is further raised up so that the device is bent by the supporting object beneath (Fig. 4A, bottom) with a radius of curvature of ~79.63 mm. The plot of measured difference in taxel currents with and without the supporting object (Fig. 4B, panel B1) illustrates a good agreement between the detected shape change of the SGVPT array and the physical shape of the supporting object beneath. The shape-adaptive sensing capability was further examined by applying an additional localized stress to the bent SGVPT array, using the same setup in Fig. 3, B and C, as depicted by the 3D schematic drawing in Fig. 4B (bottom right). The measured variation in taxel current values between the bent SGVPT array with extra stress and the unstrained SGVPT array is shown in Fig. 4B (panel B2). A clearer demonstration of the data can be obtained by numerical subtraction (Fig. 4B, panel B2–B1), which gives rise to spatial imaging of the additionally applied stress when the shape of the SGVPT device changes. Such shape-adaptive sensing has

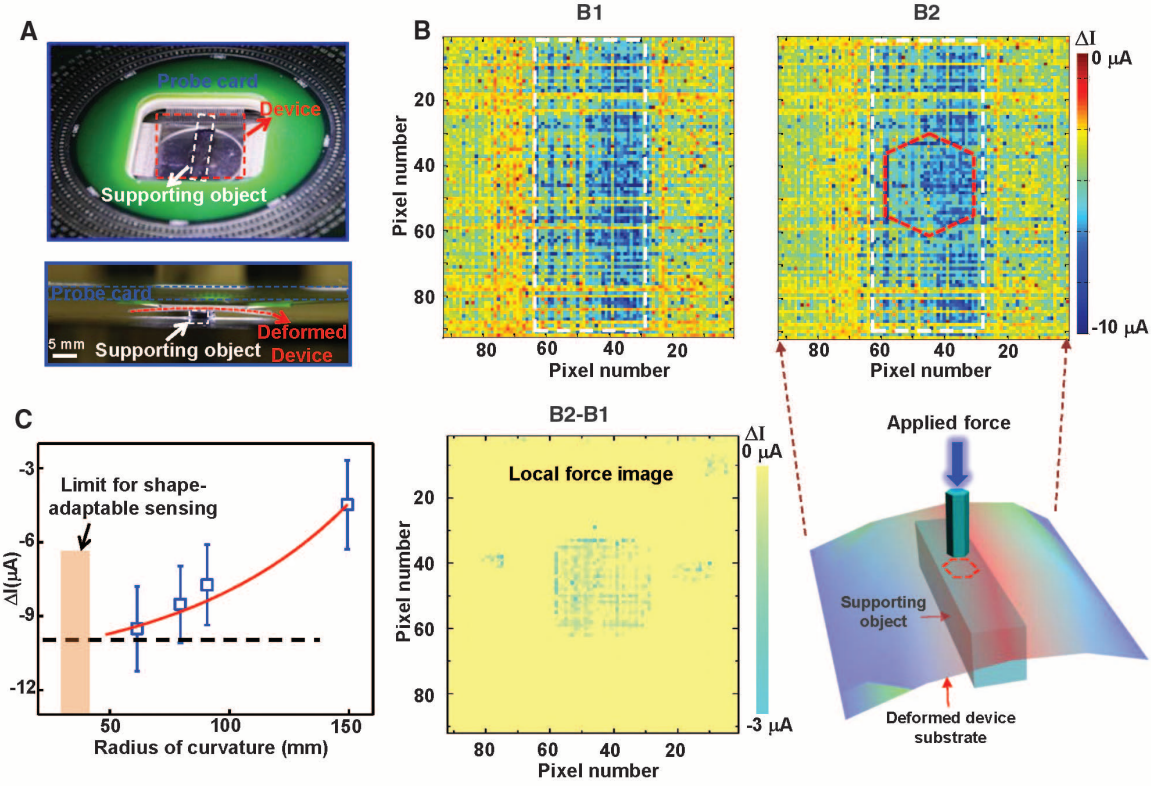

Fig. 4. Shape-adaptive sensing by the flexible 92 × 92 SGVPT array. (**A**) Photographs of the experimental setup for investigating the feasibility of a SGVPT array for shape-adaptive sensing. Upper image, top view; lower image, side view with the device deformed. (**B**) Shape-adaptive sensing of the SGVPT array. (B1) The measured difference in taxel currents for the SGVPT array with and without a supporting object beneath. The detected shape change of the SGVPT array is illustrated by the dark blue regions; the physical shape of the supporting object beneath the SGVPT device is outlined by the white dashed lines. (B2) The measured variations in taxel current values between bent the SGVPT array with extra stress and the unstrained SGVPT array. The location of the extra stress is outlined by the red dashed lines. (B2–B1) A clearer demonstration of the data is obtained by numerically subtracting B1 from B2, giving rise to spatial imaging of the additionally applied stress when the shape of the SGVPT device is changed. The 3D schematic drawing at the lower right illustrates the process for shape-adaptive sensing. (**C**) Experimental results show the limit for shape-adaptable sensing by a SGVPT array with the present design.

also been investigated for other radii of curvature (fig. S11). Because of the relatively large thickness of the SGVPT device (mainly contributed by the polyethylene terephthalate substrate, which is 500 μm thick), the saturation of SGVPT response under high pressure (as shown in Fig. 2C), and the constraints of the measurement setup (e.g., limited vertical movement of probes), the SGVPT array is unable to sense the change in device shape and further distinguish the applied pressure when the radius of curvature is smaller than 30 to 35 mm (Fig. 4C). The detectable range of shape deformation (and of the corresponding shape-adaptive sensing) can be improved by engineering the device into more compliant form to reduce the strain induced in the SGVPT as a result of changes in device shape (fig. S12).

A SGVPT array was repeatedly bent to a very small radius of curvature (15 mm, as shown in fig. S13) at a frequency of 2 Hz to simulate accelerated aging. Metrology mapping was then performed on the array and plotted for comparison with that of the device before the cyclic bending. No obvious degradation in SGVPT array operation could be observed even after 1000 cycles of bending, suggesting good reliability and stability in device operation.

The SGVPT devices described above can function as active and self-powered tactile sensors by directly converting applied mechanical actuations into electrical control signals without applying gate voltage (fig. S14). Hence, they can act as a fundamental component for piezotronics (*15*, *25*).

References and Notes

1. K. Takei *et al.*, *Nat. Mater.* **9**, 821 (2010).
2. S. C. B. Mannsfeld *et al.*, *Nat. Mater.* **9**, 859 (2010).
3. T. Someya *et al.*, *Proc. Natl. Acad. Sci. U.S.A.* **101**, 9966 (2004).
4. D. J. Lipomi *et al.*, *Nat. Nanotechnol.* **6**, 788 (2011).
5. D. H. Kim *et al.*, *Science* **333**, 838 (2011).
6. T. Sekitani *et al.*, *Science* **326**, 1516 (2009).
7. D. H. Kim *et al.*, *Science* **320**, 507 (2008).
8. A. Javey, S. Nam, R. S. Friedman, H. Yan, C. M. Lieber, *Nano Lett.* **7**, 773 (2007).
9. J. H. Ahn *et al.*, *Science* **314**, 1754 (2006).
10. S. Nam, X. C. Jiang, Q. H. Xiong, D. Ham, C. M. Lieber, *Proc. Natl. Acad. Sci. U.S.A.* **106**, 21035 (2009).
11. T. Bryllert, L. E. Wernersson, L. E. Froberg, L. Samuelson, *IEEE Electron Device Lett.* **27**, 323 (2006).
12. J. Zhou *et al.*, *Nano Lett.* **8**, 3973 (2008).
13. W. Z. Wu, Y. G. Wei, Z. L. Wang, *Adv. Mater.* **22**, 4711 (2010).
14. Z. L. Wang, *Adv. Mater.* **19**, 889 (2007).
15. Z. L. Wang, *Piezotronics and Piezo-Phototronics* (Springer, New York, 2013).
16. Z. L. Wang, *Nano Today* **5**, 540 (2010).
17. Y. Zhang, Y. Liu, Z. L. Wang, *Adv. Mater.* **23**, 3004 (2011).
18. Z. L. Wang, *Adv. Mater.* **24**, 4632 (2012).
19. W. Z. Wu, Z. L. Wang, *Nano Lett.* **11**, 2779 (2011).
20. J. Shi, M. B. Starr, X. D. Wang, *Adv. Mater.* **24**, 4683 (2012).
21. R. S. Johansson, A. B. Vallbo, *J. Physiol.* **286**, 283 (1979).
22. Y. G. Wei *et al.*, *Nano Lett.* **10**, 3414 (2010).
23. B. Nemeth *et al.*, *Adv. Mater.* **24**, 1238 (2012).
24. S. A. Mascaro, H. H. Asada, *IEEE Trans. Robot. Autom.* **17**, 698 (2001).
25. Z. L. Wang, W. Z. Wu, *Angew. Chem. Int. Ed.* **51**, 11700 (2012).

Acknowledgments: We thank Y. Zhang for helpful discussions and P. Shao for guidance in using the optical noncontact profilometer. Supported by the Defense Advanced Research Projects Agency, U.S. Air Force, U.S. Department of Energy, Office of Basic Energy Sciences (award DE-FG02-07ER46394), NSF, and the Knowledge Innovation Program of the Chinese Academy of Sciences (grant KJCX2-YW-M13).

Supplementary Materials

www.sciencemag.org/cgi/content/full/science.1234855/DC1
Materials and Methods
Figs. S1 to S16

7 January 2013; accepted 5 April 2013
Published online 25 April 2013;
10.1126/science.1234855

Periodic Segregation of Solute Atoms in Fully Coherent Twin Boundaries

J. F. Nie,[1]* Y. M. Zhu,[1] J. Z. Liu,[2] X. Y. Fang[3]

The formability and mechanical properties of many engineering alloys are intimately related to the formation and growth of twins. Understanding the structure and chemistry of twin boundaries at the atomic scale is crucial if we are to properly tailor twins to achieve a new range of desired properties. We report an unusual phenomenon in magnesium alloys that until now was thought unlikely: the equilibrium segregation of solute atoms into patterns within fully coherent terraces of deformation twin boundaries. This ordered segregation provides a pinning effect for twin boundaries, leading to a concomitant but unusual situation in which annealing strengthens rather than weakens these alloys. The findings point to a platform for engineering nano-twinned structures through solute atoms. This may lead to new alloy compositions and thermomechanical processes.

Interfaces such as twin and grain boundaries play a critical role in plastic deformation and ultimately in controlling the formability and mechanical properties of many engineering materials (*1*–*5*); notable examples are lightweight magnesium (Mg) alloys, which have received considerable attention for applications leading to fuel efficiency and green environment (*6*). Like other commonly used metals such as titanium (Ti), zirconium (Zr), and zinc (Zn), Mg has a hexagonal structure with fewer slip systems than those of cubic materials. To readily form Mg products requires the activation of twinning modes for plastic deformation. As an emerging class of engineering materials, Mg alloys are less strong than the counterpart aluminum alloys, implying the need for more efficient barriers in order to impede the motion of dislocations and twin boundaries. The control of deformation twinning during thermomechanical processes and applications is a major technical barrier to the wider application of Mg (*7*). Twinning occurs predominantly in the $\langle\bar{1}011\rangle\{10\bar{1}2\}$ system (where $\{10\bar{1}2\}$ is the twinning plane and $\langle\bar{1}011\rangle$ is the twinning direction in the twinning plane), although $\langle\bar{1}012\rangle\{10\bar{1}1\}$ and $\langle\bar{3}032\rangle\{10\bar{1}3\}$ have also been observed (*8*–*13*). The formability, yield strength, and tension–compression yield-strength asymmetry of wrought Mg products are all intimately related to twinning; hence, there have been considerable efforts to gain a fundamental understanding of the nucleation, growth, and thermal stability of such deformation twins and of the factors that dictate their development under different loading conditions. However, gaining fundamental insights from experimental observations of the effects of solute, second-phase particles, grain size, and sample size on deformation twinning in Mg (*14*–*16*) has proved elusive. This has also been the case more broadly in engineering materials (*17*–*19*). Specifically, we need atomic-scale experimental evidence and an understanding of the structure and chemistry of twin boundaries in alloys.

In contrast with partially coherent interfaces such as high-angle grain boundaries and symmetrical tilt boundaries with arrays of misfit dislocations, for which segregation of alloying elements is well established (*20*–*22*), fully coherent twin boundaries have low interfacial energies, and solute segregation in such boundaries is therefore not expected. We studied this issue using high-angle annular dark-field scanning transmission electron microscopy (HAADF-STEM) to observe the migration and segregation of randomly distributed solute atoms to fully coherent terraces of deformation twin boundaries in Mg alloys. Solutes consisted of gadolinium (Gd) (which is larger than Mg and represents rare-earth elements that are major alloying additions in many commercial Mg alloys), Zn (which is smaller than Mg and a major alloying element in some commonly used Mg alloys), and mixtures of Gd and Zn (table S1). We also analyzed the experimental observations using first-principles calculations (fig. S1) and continuum estimates and the impact of the solute segregation on mechanical properties using compression tests. Alloy compositions, the preparation and testing conditions and characterizations, and the details of the computations are available in the supplementary materials.

[1]Department of Materials Engineering, Monash University, Victoria 3800, Australia. [2]Department of Mechanical and Aerospace Engineering, Monash University, Victoria 3800, Australia. [3]Monash Centre for Electron Microscopy, Monash University, Victoria 3800, Australia.

*Corresponding author. E-mail: jianfeng.nie@monash.edu